# OPERATING A FULL TUNGSTEN ACTIVELY COOLED TOKAMAK: OVERVIEW OF WEST FIRST PHASE OF OPERATION

J. BUCALOSSI CEA, IRFM F-13108 St-Paul-Lez-Durance, France Email: jerome.bucalossi@cea.fr

**WEST TEAM\*** 

\*http://west.cea.fr/WESTteam

## **Abstract**

WEST is a MA class superconducting, actively cooled, full tungsten (W) tokamak, able to operate in long pulses up to 1000 s. In support of ITER operation and DEMO conceptual activities, key missions of WEST are: i) qualification of the high heat flux plasma facing components in integrating both technological and physics aspects in relevant heat and particle exhaust conditions, particularly for the tungsten monoblocks foreseen in ITER divertor; ii) integrated steady state operation, with a focus on power exhaust issues. During the phase 1 of operation (2017-2020), a few prototypes of ITER-grade plasma facing units were integrated into the inertially cooled W coated startup lower divertor. Up to 9 MW of RF power has been coupled to the plasma and divertor heat flux of up to 6 MW/m² were reached. Long pulse operation was started with a discharge of about one minute achieved using the actively cooled upper divertor. This paper gives an overview of the results achieved in phase 1, including exposure of first ITER-grade plasma facing units. Perspectives for phase 2, operating with a full ITER-grade lower divertor, are also evoked.

### 1. INTRODUCTION

The concept of a superconducting tokamak, equipped with actively cooled metallic plasma-facing components (PFC), is today one of the options for the development of fusion energy. Integration of both physics and

technology to control steady-state plasmas in such an environment is an essential step to prepare the operation of the future fusion reactor. For this purpose, WEST was built with international partners from China, Europe, India, Korea, and USA. WEST is a MA class superconducting tokamak (plasma current  $I_p = 0.5-1$  MA, toroidal field B = 3.7 T, major radius R = 2.5 m, minor radius a = 0.5 m), equipped with two updown symmetric divertors. PFCs are all tungsten and actively cooled [1].WEST is able to operate long pulses up to 1000 s [2] (Fig.1) with high particle fluence, thanks to its RF heating and current drive systems: 9 MW of Ion Cyclotron Resonance Heating (ICRH) [3], [4], and CW 6 MW of Lower Hybrid Current Drive (LHCD) [5]. The key mission of WEST is to prepare ITER operation, but also to support the conceptual activities in view of DEMO. It aims at paving the way towards the ITER actively cooled tungsten divertor procurement and operation; and at mastering integrated plasma scenario over relevant plasma wall equilibrium time scale in a full tungsten environment. Power exhaust in long and steady-state pulses can be studied in various divertor configurations: lower single null

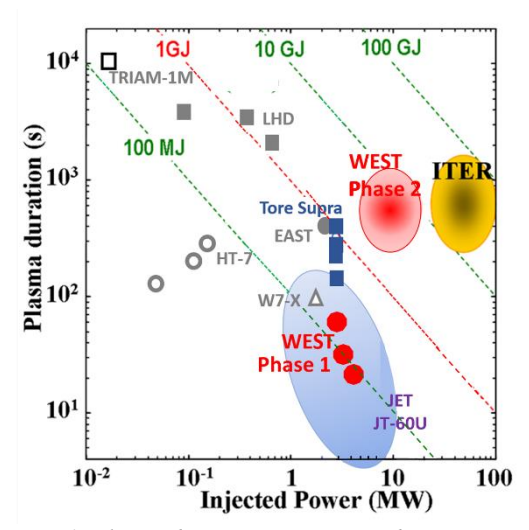


Fig. 1: Plasma duration versus injected power in various long pulse devices.

(LSN), upper single null (USN) and double null (DN). For the phase 1 of operation from 2017-2020, the lower divertor is composed of a set of ITER-grade Plasma Facing Units (PFU) based on the W monoblock concept, complemented with inertially cooled W-coated elements. For the phase 2, from summer 2021, the lower divertor will be fully ITER-grade (456 PFUs). This paper reports the main findings from the exploitation in phase 1 related to the operational domain, plasma scenario, plasma wall interaction (PWI) and first tests of the ITER-grade PFU.

The paper is organized as follows. Section 2 describes the plasma operation and monitoring systems for PFCs. Plasma scenario development towards long pulses is reported in Section 3. Section 4 details the analyses of plasma wall interaction. Section 5 is devoted to tests of ITER-grade PFU. Finally, the conclusions and perspectives towards WEST phase 2 in the context of ITER operation preparation and DEMO conceptual design are given in Section 6.

#### 2. PLASMA OPERATION AND MONITORING SYSTEMS FOR PLASMA-FACING COMPONENTS

Protection of plasma facing components is crucial when operating devices in long pulses with injected power at multi-megawatts levels. In WEST, the power loads on PFCs are expected to be in the range of those in ITER: 10-20 MW.m<sup>-2</sup>. Various diagnostics are installed for monitoring and inspection (Fig. 2). An infrared (IR) thermography system is implemented **Erreur! Source du renvoi introuvable.**, enabling real-time (RT) monitoring of PFC surface temperature to ensure safe operation while providing essential data for PWI physics studies. This IR system consists of a set of three different diagnostics: 7 endoscopes located in upper ports devoted to machine protection, covering the lower divertor and the five RF antennas; a tangential wide-angle camera covering 1/6 of the vacuum vessel, and in particular upper port protections, upper divertor targets, bottom divertor baffle, and inner guard limiter; a very high-resolution view (100µm pixel size) of the lower divertor. The data produced by the IR system is visualized and analysed with the versatile ThermaVIP software (Viewing Imaging Platform) [7], and routinely used for real-time processing of PFC temperature monitoring [8]. For about 14% of the pulses, the IR monitoring led to a thorough reduction of the heating systems injected power, and thereby helped to protect the PFCs, while allowing plasma discharges continuation.

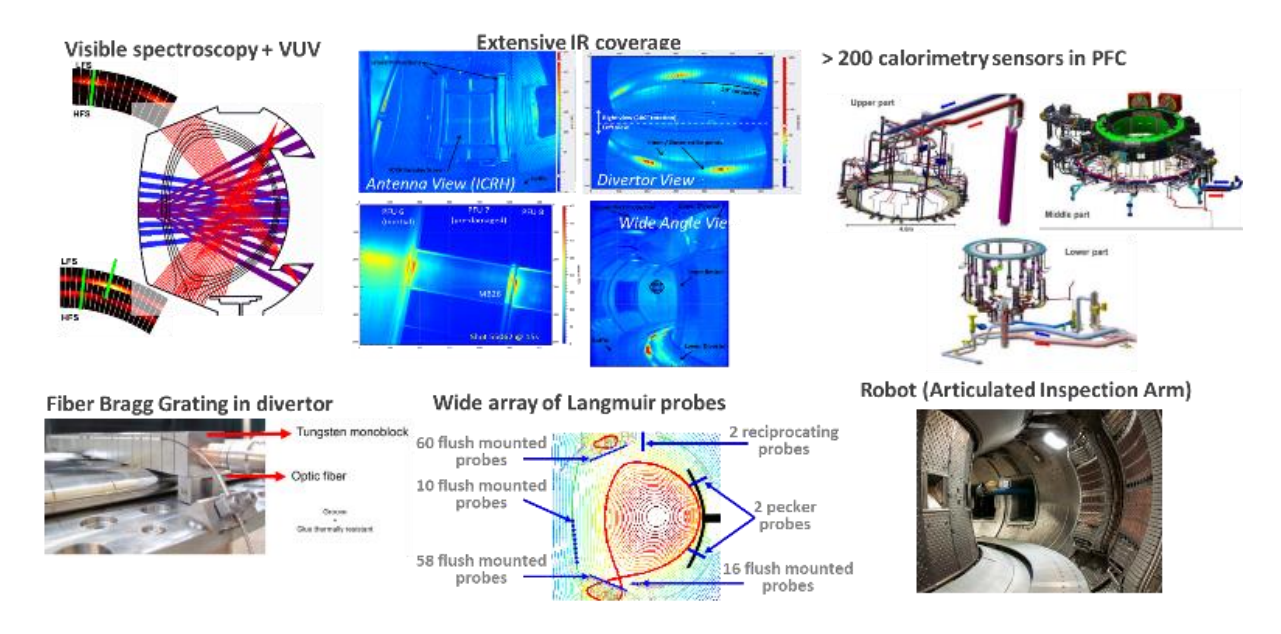


Fig. 2: Diagnostics devoted to monitoring and inspection of PFCs

An example of such active RT protection using IR cameras is illustrated in Fig. 3. In this figure, we can see that

the temperature of the PFC has exceeded the safety threshold during the power ramp of the LHCD, preprogrammed at 2MW. Active LHCD power control was then triggered in order to keep the PFCs safe, below the critical temperature. It is worth noting that thanks to this reliable RT monitoring, no water leak occurred during phase 1 of operation. All water-cooled elements facing the plasma are also monitored by calorimetry diagnostic composed of more than 200 sensors [9]. So far, heat flux distribution on the overall plasma vacuum vessel is analyzed 5 minutes after plasma discharge, which will be implemented in wall plasma monitoring system for RT control. Moreover, several specific diagnostics are dedicated to PWI and W transport studies, such as a wide array of Langmuir probes (LP) [10], Fibber Bragg Grating (FBG) [11], visible (~240 lines of sight)/VUV spectroscopy, a robotic Articulated Inspection Arm (AIA) [12] (Fig. 2).

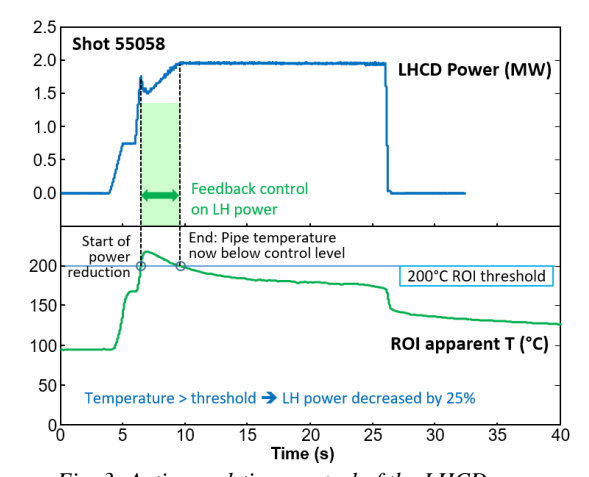


Fig. 3: Active real-time control of the LHCD power, using IR system, to avoid the overheat of PFCs

In the initial commissioning phase of WEST, large number of runaway electrons (RE) were produced at the early stage of the discharge and attributed to the high level of impurities that considerably narrowed the operational

window in which burn-through was achievable [13]. Too low prefill pressure led to non-sustained breakdowns, as expected, while unexpectedly, too high prefill led to runaway electrons. Machine conditions explained this behaviour, as RE discharges exhibited higher radiated fractions in the first 25 ms after breakdown. In those situations, the ohmic current fails to rise quickly enough, and the available flux change from the central solenoid is preferentially taken by runaway electrons seeds. In a superconducting device, runaways electrons can seriously damage the superconducting magnets, not only the PFCs. Indeed, in a discharge performed at 350 kA, RE appeared during plasma current ramp-up then stayed during the whole current flat-top phase. They were ultimately lost, after the plasma disruption, on the protection limiters of RF antennas, generating a cone of photoneutrons that triggered the quench of the toroidal field (TF) coil in its trajectory. Analyses of this quench event and the detection system are reported in [14]. RE production during plasma breakdown, ramp-up and disruptions can therefore be a serious threat to the reliability and availability of ITER and future fusion devices.

The first boronization of the vessel walls considerably improved breakdown conditions by almost completely suppressing RE beam formation. In addition, it opened the operational domain to densities well above the  $1.5 \times 10^{19} \text{m}^{-3}$  limit encountered before the first boronization. The usual reduction of intrinsic oxygen contamination was observed as well as the reduction of the associated strong edge radiation level but at the expense of tungsten core radiation as discussed later.

### 3. PLASMA SCENARIO DEVELOPMENT

Most of WEST experiments, in which the electron heating is dominant, were performed in LSN and USN configurations at magnetic field 3.6-3.7 T, R ~ 2.5 m, a ~ 0.45 m,  $\kappa$  ~ 1.3,  $\delta \sim 0.5$ , plasma current in the range of 0.3-0.7 MA (q95 ~ 3-6) and up to 1 MA, central from 2.5-8.5×10<sup>19</sup>m<sup>-3</sup> electron density (Greenwald fraction = 0.3-0.8) [15]. RF power is provided by two LHCD launchers and three ICRH load resilient antennas [4]. All the ICRH antennas and LHCD launchers are actively cooled, being able to operate in CW. They are movable radially for optimizing the power coupling and thermal loads handling. The LHCD launchers are based on the Fully Active Multijunction and Passive Multijunction. The latter is able to couple the power at long distance from the plasma [16]. So far, the LHCD and ICRH powers coupled 5.3 MW and 5.7 MW reached respectively. The total injected power has

8 6 P<sub>LHCD</sub> (MW) 4 P<sub>ICRH</sub> (MW) 2 RAD (MV 0 n<sub>e</sub> (10<sup>20</sup>m<sup>-2</sup> 0.4 W<sub>MHD</sub> (MJ) 0.3 0.2 D-D neutrons (10<sup>13</sup>/s 0.1 10 12 8 Time (s)

Fig.4: time traces of pulse 55799 run at 500kA. Upper panel shows the total RF, LHCD, ICRH and radiated powers; lower panel shows the line averaged electron density, the energy content from MHD equilibrium and the D-D neutron rate.

reached a peak of 9 MW. Fig. 4 illustrates a pulse with the 5 antennas active and a total RF power of 8 MW. The fraction of radiated power is generally 50-55% in the range of parameters explored [15]. It has to be noted that

the 5 antennas are equipped with W coated side limiters. Interestingly, the fraction of radiated power is very similar when operating LHCD or ICRH, despite ion acceleration in front of the ICRH antennas favouring W sputtering [17]. Discharges lasting more than 30 s were routinely carried out. Discharge duration close to 1 minute was obtained with 3 MW of LHCD power alone (Fig.6a) using the actively cooled upper divertor.

As already observed in several experiments with metallic PFCs (e.g., FTU [18], JET [19]), achieving a reliable plasma current ramp-up can be challenging due to the risk of large core radiation, and subsequent triggering of MHD

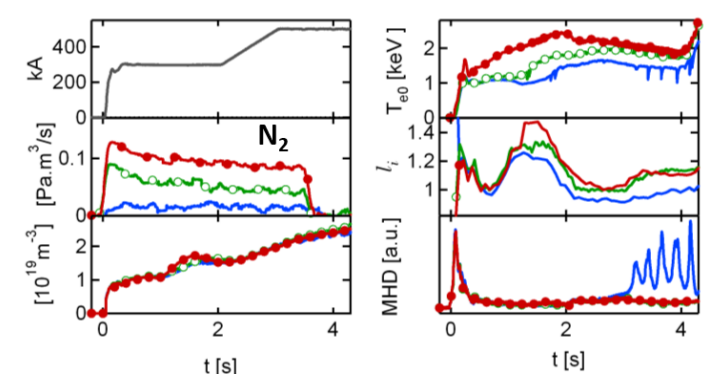
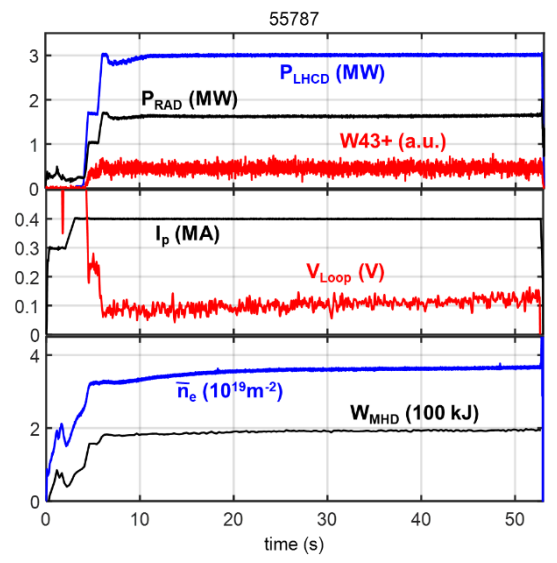


Fig.5: Example of 3 consecutive pulses (54762, 54764, 54765) with increasing Nitrogen seeding rate. Left column: plasma current (top), Nitrogen injection rate (middle) and volume averaged plasma density (bottom). Right column: central electron temperature, internal inductance and MHD level.

modes. In WEST, during the early plasma current ramp up, tungsten central radiation very often cools down the plasma in the centre that lead to hollow electron temperature ( $T_e$ ) profile and triggers MHD 2/1 mode. One needs therefore a central heating method. Electron Cyclotron Resonance Heating (ECRH) method is a well suited candidate as it is able to couple the power in the very early phase of current ramp up. A 3MW/CW ECRH system is under preparation for WEST phase 2 of operation. In the meantime, another technique to avoid  $T_e$  hollow profile is used in WEST. It consists in injecting nitrogen during the current ramp-up (Fig. 5) [20].  $N_2$  injection induces an increase of the plasma resistivity in the peripheral region that leads to faster current diffusion (see plasma inductance in Fig. 5), hence higher ohmic heating in the centre which compensates for the plasma cooling due to W core radiation.

Tungsten is, in most cases, the major radiating species but tungsten accumulation is generally not an operational issue on WEST as illustrated for a 53 s pulse on (Fig.6a). This experimental observation is consistent with simulations and could be explained by low torque plasmas in WEST. Indeed, transport simulations computed with GKW and NEO reported in [21], figured out that W neoclassical transport is dominant only within the very core region r/a < 0.25. Hence, despite unfavourable peaked electron density profile, the radial profile of tungsten is



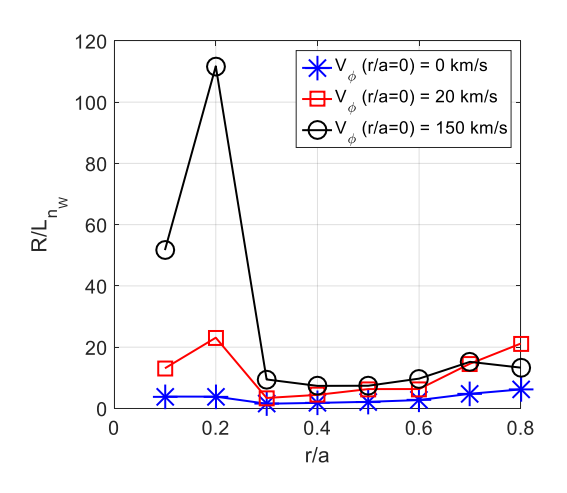


Fig.6a: Discharge sustained by LCD (3.7T/0.4 MA, USN configuration)

Fig.6b: Normalized W density gradient length for various toroidal rotation velocity.

predicted to be rather flat (Fig. 6b). Note that the W peaking would significantly increase in presence of a large toroidal rotation (Fig. 6b) that is not expected in WEST RF heated plasma. This result is promising for ITER low torque operation.

L-mode discharges in WEST exhibit an H factor around 0.8 with respect to the H-mode scaling H98,y2 as shown in Fig 7 with ITPA-IOS database for metallic devices [22]. This surprising results for L mode plasmas is due to the unfavourable aspect ratio dependence of the H98 scaling law, leading to, at A = 5-6, similar confinement time

prediction using the L96 or the H98 scaling laws. The weak aspect ratio dependence of the L96 scaling law is confirmed. Adding more than 1000 WEST entries modifies the exponent to A from 0.04 in the L96 scaling to 0 if performing the regression including **WEST** [23]. entries Concerning H-mode scaling laws, IPB98(y,2) report a degradation of confinement with A, DS03 report a benefit of working at large A [24]. The relatively narrow range of the available A parameters in the databases which are used for energy confinement time scaling laws likely explains this opposite trend. Given this uncertainty, it is worth exploring H-mode confinement in large A devices such as WEST.

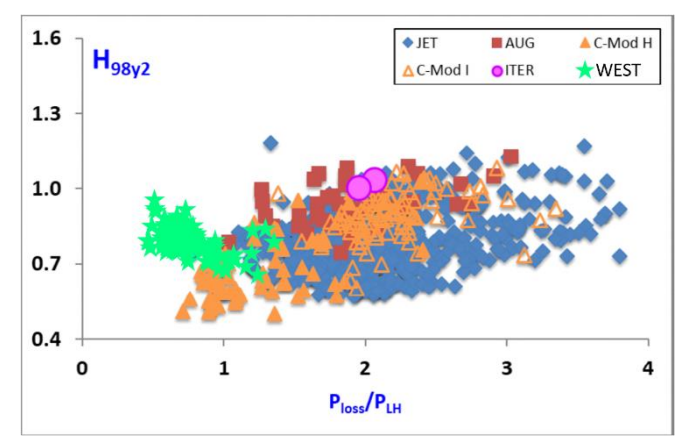


Fig.7: H factor in metallic devices from ITPA-IOS database showing WEST discharges during phase 1 of operation

Up to now, H-mode has been obtained in WEST only after fresh boronization when the radiated fraction is reduced down to 30% for several discharges. L-H transitions were observed when the power crossing the separatrix is between 3-3.5 MW as expected by the ITPA empirical scaling law [25]. When combining 4 MW of LHCD with 1 MW of ICRH, the ExB velocity profile exhibits a deeper well, reaching -5 km/s [26] (Fig 8) together with a steepening of edge density measured by fast sweeping reflectometry (Fig. 8). It results in a significant increase of the particle confinement time; 30% increase of plasma density when the gas injection is turned off. The increment in the energy content is weaker, less than 10%, and no ELMs have been observed. Moreover, in most cases, the plasma radiation increases leading to an oscillatory regime. During phase 1 of operation, the available power and the core radiation level mainly due to W contamination has limited the plasma regimes close to the LH threshold. Heating power should progress in phase 2 and allow for easier burn though of W radiation and facilitate access to H-mode operation.

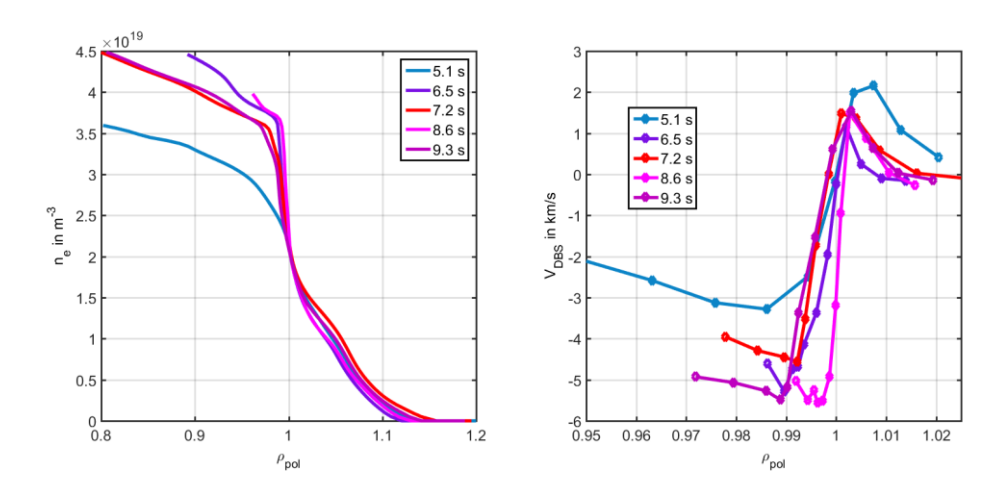


Fig. 8: Density profile evolution (left) and ExB velocity profile (right) from fast sweeping reflectometry during WEST pulse 55564.

## 4. PLASMA WALL INTERACTION STUDY

One of the main goals of WEST is the assessment of power handling capabilities and lifetime of tungsten divertor components under high heat flux and high fluence operation in a full W tokamak environment. During its phase 1, WEST operated with a lower divertor composed of a set of actively cooled ITER-grade tungsten PFUs and inertial tungsten coated graphite components. Characterization of this divertor has been performed notably by using a large set of divertor diagnostics such as thermocouples (TC), flush-mounted Langmuir probes (LP) and Fibber Bragg Grating (FBG) embedded in the W-coated graphite components (Fig. 9).

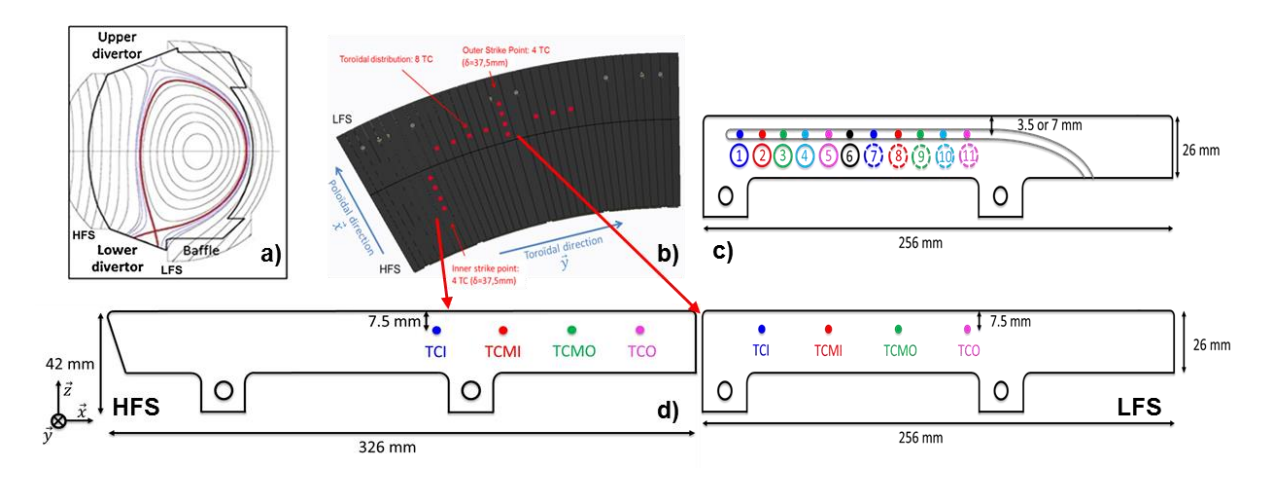


Fig. 9: a) Poloidal magnetic field configuration (Far X-Point) in the WEST Tokamak. b) Top view of the lower divertor instrumented with 16 TC (red points). c) 2D poloidal cross section of the PFC with FBGs (the surface exposed to the plasma is on the top). d) 2D poloidal cross section of the two PFC with 4TCs.

Heat flux deposition on the W-coated graphite components of lower divertor has been studied in detail in [27] using the whole set of measurements. The study includes a large database of L-mode plasmas heated by LHCD and/or ICRH, up to 8 MW total injected power during 4 seconds and up to 90 MJ total injected energy in lower single null configuration (Fig. 10). An asymmetry between the outer and inner heat flux is reported: 3/4 1/4 distribution for the parallel heat load, as expected with the drift flows in forward magnetic field [28]. Deposited heat flux on the lower divertor has reached 6 MW/m² at the outer strike point (OSP), as shown in Fig. 10a. As expected, the heat flux decay length at the target varies almost linearly with the magnetic compression of the field lines, from 60 mm for low compression down to 10 mm for high compression (Fig. 10b). The maximal deposited heat flux observed so far, about 6 MW/m², has been obtained with 4 MW of LH power, a radiated fraction of 45% and a X-point height of 120 mm showing that the 10 MW/m² could be achieved with about 7 MW of additional power and 50% of power radiated in this L-mode configuration. Hence, extrapolation from achieved results indicate that WEST will provide heat flux in the range of 10-20 MW/m² when it operates, even in L-mode, at full heating capability of 15 MW thanks to the flexibility allowed by the X-point height variation (up to 120 mm).

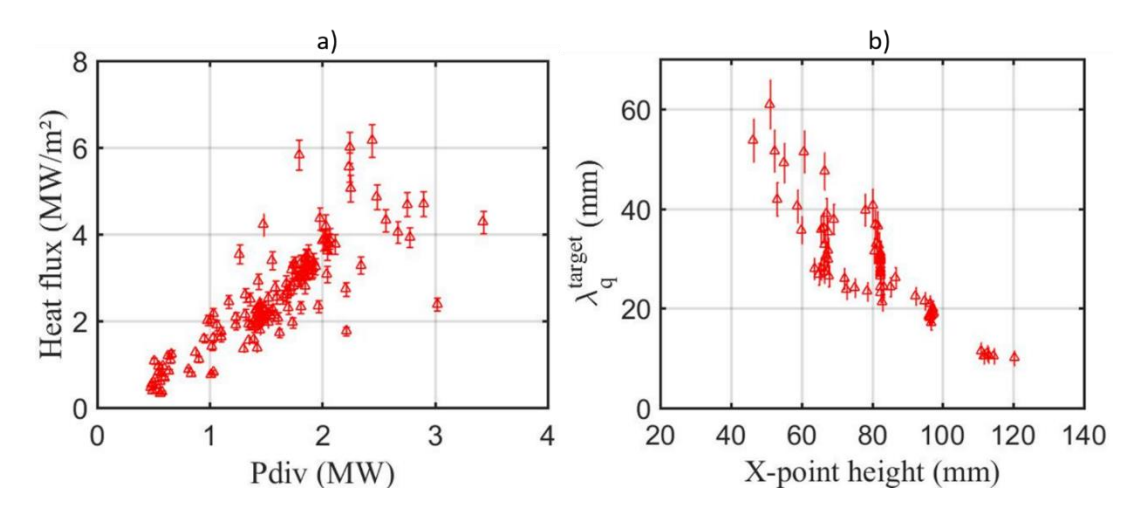


Fig. 10: a) Outer strike point heat flux versus divertor with total injected power up to  $6MW/m^2$  (Pdiv = Ptot - Prad); b) Heat flux decay length versus X-point height from TC measurements (at Ip = 0.5 MA)

Analyse of IR exhibits a complex spatial distribution of effective emissivity on the divertor (Fig. 11), which is correlated with erosion/redeposition pattern. Effective emissivity is about 0.12 in outer strike points regions, consistent with pristine inertial PFU. The emissivity map evolves significantly over the campaign adding significant complexity to the real-time protection system of the divertor.

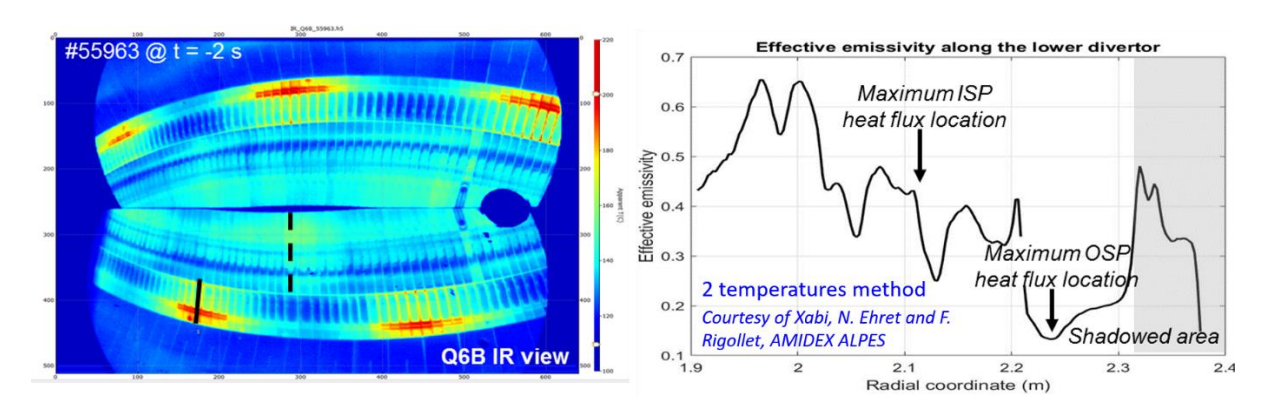


Fig. 11: Infrared image showing two 30° sectors of the lower divertor (optically recombined on one camera) (left) and estimated effective emissivity along the W-coated tiles in the poloidal direction (right)

A procedure, described in [29], was implemented to estimate, for a given pulse, a given infra-red endoscope and a given tile equipped with thermocouples, profiles of effective emissivity and background reflections. Using this procedure on infrared data before implementing thermal inversion [29], one can compute the heat flux profile along the tile. Both FBG and IR gives an estimate of the heat channel width at the target that can be remapped to the midplane by normalization with the magnetic flux expansion. Estimates with FBG are systematically higher

than estimates with IR: about 2.8 mm was found with the IR method while about 7.2 mm with the FBG method. For comparison, L-mode scaling laws for this case predicts  $\lambda_q = 2.9-3.7$  mm.

Plasma edge simulations using the SOLEDGE2D-Eirene code package have been performed and divertor in/out asymmetries are well reproduced [30] and [31]. Simulations were performed for a series of discharges at Ip = 0.5 MA, with 4 MW of injected power, 2.3 MW of total radiated power, 4x10<sup>19</sup> m<sup>-2</sup> of central line integrated density and a height of the X point of about 115 mm from the wall. As shown in Fig. 12, SOLEDGE results are in good agreement with the density and temperature profiles measured by Langmuir probes embedded in the divertor. Total radiated power of 780 kW is in quantitative agreement with the bolometry measurements in the divertor region. Simulations also show a strong asymmetry between oxygen concentrations at the inner divertor target with respect to the outer one. This asymmetry is observed by the VUV spectroscopy system using a moving line of sight in the poloidal plane, allowing one to retrieve the information on the angular position of the oxygen light emission (Fig. 13). The force balance analysis shows that friction dominates over thermal gradient forces at the inner target, while, at the outer target, the repelling thermal gradient forces dominate.

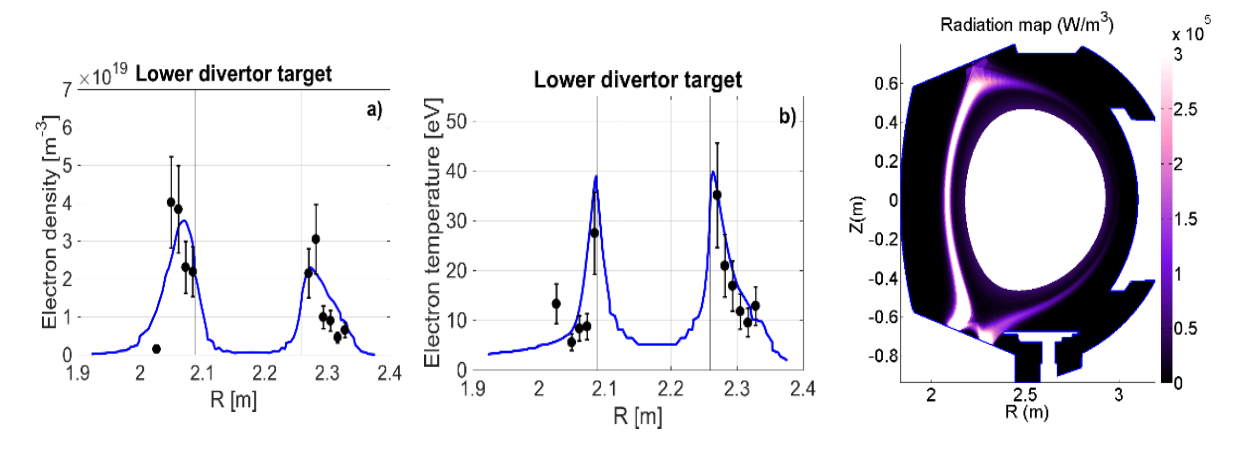


Fig. 12: Left and central panels: profiles of respectively electron density and electron temperature at the lower divertor target for the WEST #54067. In blue solid line SOLEDGE2D simulation, in black symbols the LP measurements. Right panel: radiation map from SOLEDGE2D simulation. The total radiated power is 780 kW in quantitative agreement with the bolometry measurements in the outer region.

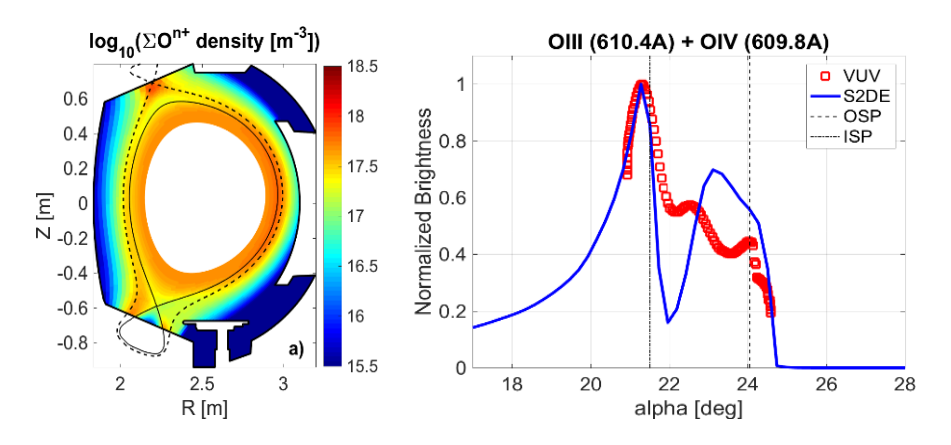


Fig. 13: Left panel: VUV system in scanning mode. Central panel: 2D poloidal map of oxygen density from SOLEDGE2D simulation. Right panel: Comparison of "poloidal" profiles of oxygen in lower divertor (not absolutely calibrated). Experimental data from VUV system are reported with red symbols while the solid blue line represents results from SOLEDGE simulation.

Concerning post mortem analysis, erosion marker tiles, featuring a thin W/Mo layer added on top of the W coating, were analysed after exposure in WEST C3 campaign. It was found that both the inner strike point (ISP) and the outer strike point (OSP) are net erosion areas, with more pronounced erosion at the OSP. The transition between strong erosion and thick deposition area is very sharp as shown on Fig 14. The C3 campaign averaged net erosion rate is roughly  $\sim 0.1$  nm/s, in the same range that what was found in AUG. Thick deposited layers (>10  $\mu$ m) were found near the ISP.

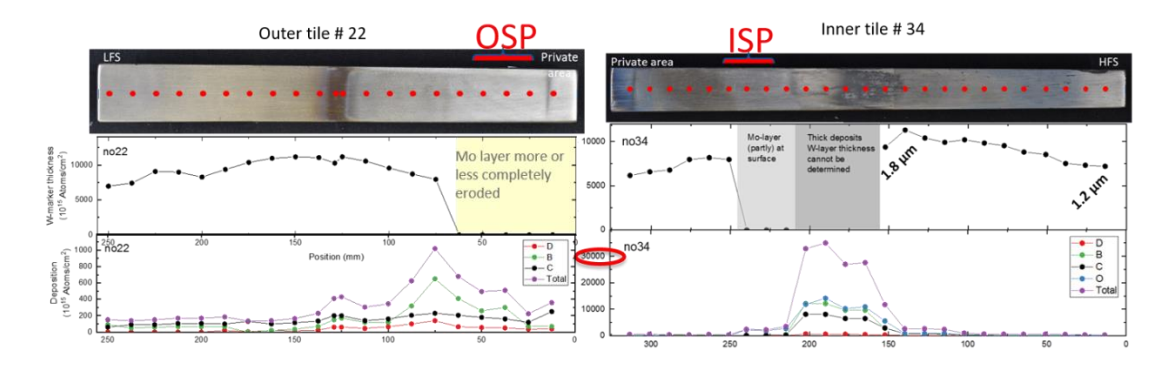


Fig. 14: post-mortem analysis of erosion marker tiles (W-coated PFU), outer tile on the left and inner tile on the right, showing the W-marker thickness on the top and the light impurity deposition on the bottom (scale is x30 on the inner tile).

ITER will operate with a tungsten divertor, a material featuring surface morphology changes when exposed to helium plasmas, in particular the formation of the so called tungsten fuzz under specific conditions. Investigating interactions between tungsten plasma facing components and helium plasmas in a tokamak environment is therefore a key point to consolidate predictions for the ITER divertor performance and lifetime. To this end, dedicated He experiments were performed in WEST at the end of the first phase of operation [32], before dismantling the lower divertor components for post mortem analysis. The experiment was designed in order to reach the conditions for W fuzz formation in the area, namely: incident particle energy  $E_{inc}>20$  eV, He fluence  $>10^{24}$  m<sup>-2</sup>, surface temperature  $>700^{\circ}$ C [33]. A robust long pulse scenario was developed in He L mode plasma with plasma current Ip = 300 kA, LHCD power = 4 MW, average density  $4\times10^{19}$  m<sup>-3</sup>. Plasma duration was adjusted to  $\sim30$  s, in order to reach a surface temperature above the threshold for W fuzz formation over a significant area around the OSP on the inertial PFUs. Repetitive He long pulses (in the range 20-30 s) were carried out, cumulating  $\sim2000$  s of plasma exposure and 4.4 GJ of energy injected to the plasma over 1 week of operation.

Local divertor plasma conditions were recorded with Langmuir probes, while the divertor surface temperature was monitored by embedded thermocouples/FBG and IR cameras. It is shown that the 3 criteria mentioned above for W fuzz formation were met in the OSP area. Indeed, typical electron temperatures measured by the Langmuir probes were  $T_e \sim 20~\text{eV}$  at the OSP as shown in Fig 15, which corresponds to an incident He energy  $E_{inc} > 100~\text{eV}$ . The temperature threshold for W fuzz formation is typically reached after 20 s at the OSP. The total He fluence reached at the OSP is assessed from cumulated Langmuir probe measurements to be  $\sim 4~10^{25}~\text{He/m}^2$ . Combining IR and LP measurements, it is shown that even in the worst case scenario (highest emissivity assumption), the threshold for W fuzz formation in terms of He fluence ( $\sim 10^{24}~\text{m}^{-2}$ )/surface temperature is reached in an area of  $\sim 1~\text{cm}$  around the OSP.

In vessel inspections using the Articulated Inspection Arm (AIA) were performed before and after the He campaign. It did not reveal any macroscopic signs of W surface modification in the OSP area of W-coated PFU, such as blackening of the surface reported when W fuzz is formed. More detailed post mortem analysis are underway and should give further insights, in particular on the presence of He nanobubbles in the near surface. It underlines however that in tokamak conditions, the complex balance between erosion/redeposition and W fuzz formation needs to be taken into account. The data obtained will be used to consolidate the experimental database supporting the modelling effort for predicting W fuzz formation and growth in ITER.

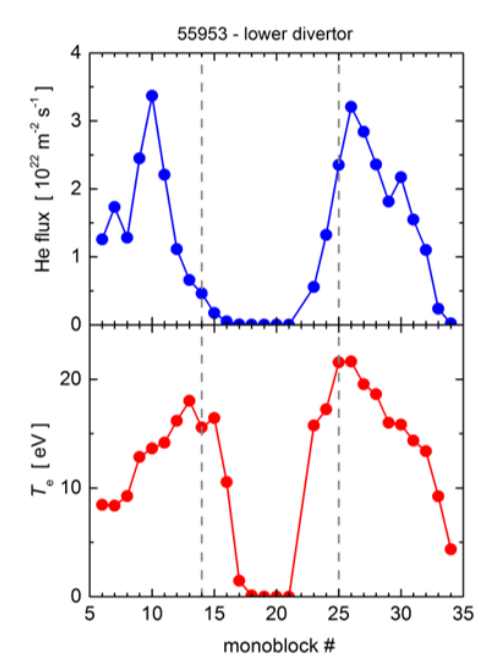


Fig. 15: cumulated He fluence (top) and electron temperature profile (bottom) estimated with Langmuir probes as a function of monoblock number along the divertor. The location of the inner and the outer strike points are shown

### 5. TEST OF ITER-GRADE PLASMA FACING UNIT

During phase 1, the WEST lower divertor was composed of a mix of ITER-grade PFU and inertially cooled, W-coated graphite PFUs. One of twelve lower divertor sectors was progressively equipped with up to 14 actively cooled ITER-grade PFUs [34], each of which has 35 monoblocks (MB) of 12 mm poloidal width separated by 0.5 mm toroidal gaps (Fig. 16).

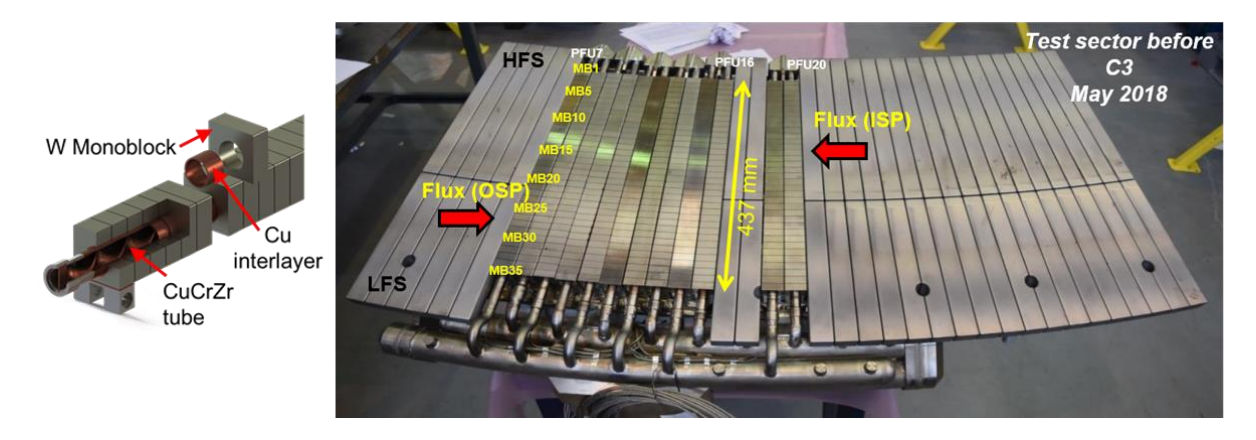


Fig.16: Photograph of the WEST lower divertor sector equipped with 12 ITER-like PFUs for the C3 campaign (2018). The poloidal length of the ITER-like PFUs (437 mm) is indicated. The remaining PFUs are made of graphite with a 15  $\mu$ m coating of W. The direction of the parallel heat flux is indicated at the inner and outer strike points (ISP and OSP).

The ITER-grade PFUs were monitored by a very-high resolution infrared camera (3.9  $\mu$ m wavelength, minimum temperature threshold ~300°C, 0.1 mm/pixel) [35]. They were not bevelled, some of them had 1 mm chamfers.

While most of the PFUs were aligned within the ITER tolerances (at most  $\pm$  0.3 mm perpendicular steps between neighbouring PFUs), three of them were not: at the OSP PFU#7, PFU#12, and PFU#19 were measured to protrude respectively +0.31 mm, +0.79 mm, and +0.63 mm above their neighbours (Fig. 17). During the C3 experimental campaign, a total of 2h30 plasma exposure was cumulated over 1076 discharges at I<sub>p</sub> up to 0.8MA lasting up to 37.5 s, corresponding to a total injected energy of 5 GJ. Auxiliary heating was mostly provided by lower hybrid antennas, coupling a maximum of 5.3 MW to the plasma. The maximum steady state surface heat load was  $q_{pk} \sim 2.5 \text{ MW/m}^2$  corresponding to parallel heat flux of q//~50 MW/m<sup>2</sup> for a typical B-field incidence angle of  $\sim 3^{\circ}$  at the outer strike point. There was a significant number of disruptions (730) and many discharges had strong MHD activity, both of which can deliver intense transient heat pulses to PFCs having durations of the order of a few ms.

The results are reported in [36] and [37]. Microscopic observations carried out after the C3 campaign revealed a variety of damage on the PFUs including cracking, optical hot spots, melting formation (Fig. 18). The damages were more severe for PFUs installed with a significant relative misalignment, for which poloidal leading edges were irradiated at near perpendicular incidence by the heat flux (measured misalignment up to 0.8 mm, to be compared with ITER specifications of 0.3 mm). The damage is observed on the full poloidal extent of the divertor, even on zones that normally should receive little or no heat flux in steady state.

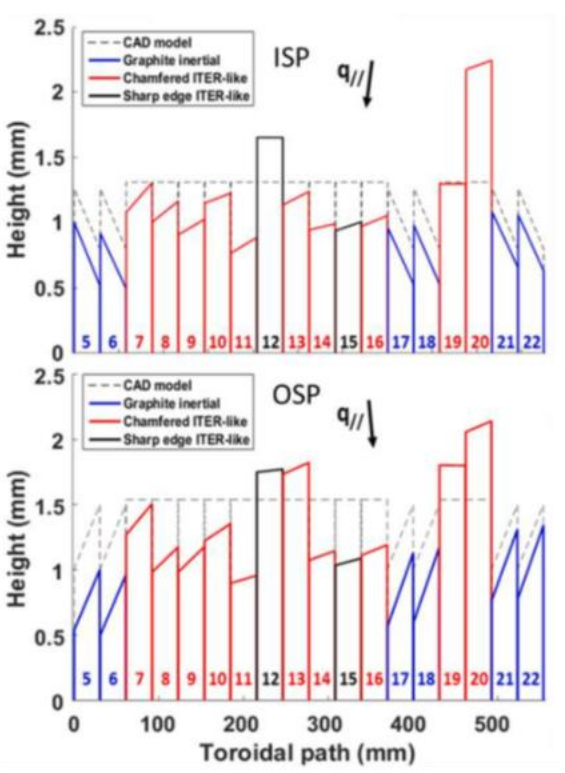
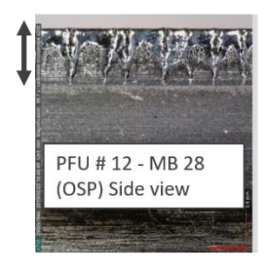
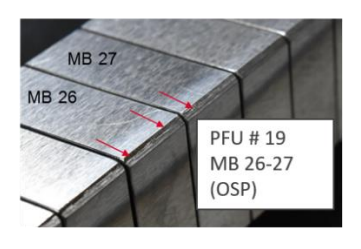


Fig.17: representation of the metrology study before C3 illustrating misalignments of the PFUs with respect to their nominal positions (dashed lines). Beveled graphite PFUs are shown in blue, chamfered W PFUs in red, and W PFUs with sharp edges in black. The ISP profile is centered on MB#17 (upper panel), and the OSP on MB#25 (lower panel). Note that the vertical scale is greatly exaggerated in order to clearly show the misalignments.







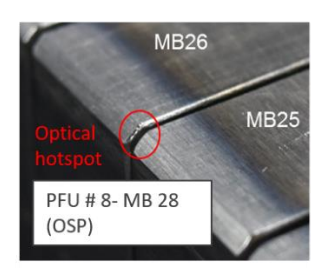
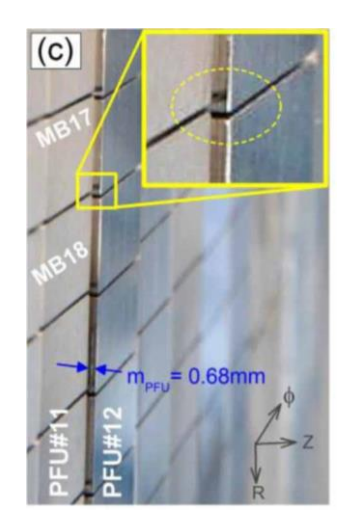


Fig.18: example of damages observed on the ITER-grade PFUs; from right to left, damage on a misaligned sharp PFU#12, on misaligned chamfered PFU#19 and on aligned chamfered PFU#8.

In particular, clear evidence of optical hot spots was observed for the first time (Fig. 19) [38], as predicted to occur in ITER in [39]. Indeed, infrared images obtained during a disruption clearly showed local heat flux deposition on isolated points of the leading edges of PFUs, as the result of penetration of charged particles into the toroidal gaps. The formation of these so-called optical hot spots were found on both chamfered and non-chamfered PFUs, as well as for PFUs misaligned and aligned.



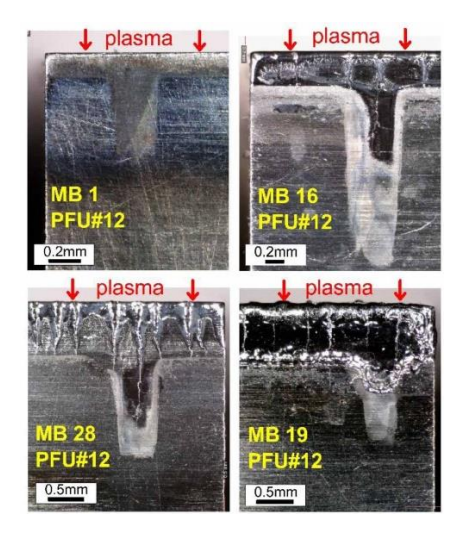


Fig. 19: evidence of optical hot spot observed on the leading edge of MB of unchamfered PFU#12. The location of the optical hot spot and the melted band are consistent with the radial and vertical misalignments of the PFU.

# 6. CONCLUSIONS AND PERSPECTIVES

WEST has completed its first phase of operation which corresponds to the first stage towards the implementation of a full ITER-grade divertor. During this phase, characterized by tungsten walls, a wide range of plasma configurations have been produced, from lower single null to upper single null and stable plasma conditions have been achieved up to 1 MA. Initial boronization played a critical role in the opening of the operational domain towards higher density and lower edge radiation but at the expense of core W radiation. RF heating with LHCD and/or ICRH, have progressed with up to 8 MW coupled to the plasma during several seconds while the radiated power fraction was found to remain around 50-55% in most of the discharges, whatever the heating mix. On the actively cooled upper W divertor, long pulses lasting up to 55 s have been routinely achieved, with no W accumulation despite peaked electron density profiles. After fresh boronization, and low core radiation, H-mode transition were observed close to the expected L-H threshold but accompanied by an increase of core radiation and an oscillatory behaviour. In the next phase of operation, higher input power will allow for exploring H-mode and I mode operational windows respectively in LSN and USN.

Concerning power handling at the divertor, asymmetries were observed with a higher impurity concentration and therefore tungsten source at the inner strike point while about ¾ of the parallel heat load was found at the outer strike point. These observations are fairly well reproduced by simulation. Scenarios with detached inner strike point offers promising developments. The heat flux level and pattern on the lower and upper divertors have been characterized thanks to embedded thermal measurements, IR and flush-mounted Langmuir Probes. The maximum heat flux currently reported is around 6 MW.m<sup>-2</sup> for 4 MW of LHCD and smallest flux expansion at the target (far

#### J. BUCALOSSI and WEST TEAM

X-point configuration) in L mode. This gives confidence to reach ITER expected divertor heat flux level in the next phase.

A set of actively cooled ITER-grade PFU have been exposed to tokamak plasmas for the first time. Cracking and local melting have been observed for misaligned PFU. In addition, optical hot spots, which have been predicted to occur in ITER at the projection of the toroidal gaps on the subsequent PFU, have been observed experimentally, even for PFU aligned within ITER specifications

The second phase of operation, with the full lower actively cooled divertor, is planned to start in summer 2021 to address long pulse/high fluence operation on the newly manufactured ITER-grade actively cooled divertor, up to 10 MW/1000 s.

#### **ACKNOWLEDGEMENTS**

This work has been carried out within the framework of the EUROfusion Consortium and the French Research Federation for Fusion Studies and has received funding from the Euratom research and training programme 2014-2018 and 2019-2020 under grant agreement No 633053. The views and opinions expressed herein do not necessarily reflect those of the European Commission.

#### REFERENCES

- [1] BUCALOSSI J. et al., 2014 Fusion Eng. Des., 89 907912
- [2] BOURDELLE C. et al., 2015 Nucl. Fusion 55 063017
- [3] BERNARD J.M. et al., 2019 Fusion Eng. Des. 146 1778-1781
- [4] HILLAIRET J. et al., this Conference TECH/3-5R
- [5] DELPECH L. et al., 2015 Fusion Eng. Des. 96–97 452–457
- [6] COURTOIS X. et al., 2019 Fusion Eng. Des., V 146 B, 2015-2020. Also at this Conference TECH/P8-18
- [7] V. MARTIN et al., Fusion Eng. Des., 86, 270 (2011)
- [8] NOUAILLETAS R. et al., 2019 Fusion Eng. Des., V 146 A, 999-1002.
- [9] LAMAISON V. et al., 31st SOFT 2020
- [10] DEJARNAC R. et al., submitted to Fus. Eng. Des. (2020).
- [11] CORRE Y. et al., Rev. Sci. Instrum. 89 (2018), 063508
- [12] VILLEDIEU E. et al., Fusion Eng. Des. https://doi.org/10.1016/j.fusengdes.2015.11.048
- [13] REUX C. et al., this Conference EX/P5-5
- [14] TORRE A. et al., 2019 IEEE Transactions on Applied Superconductivity 29, 5 4702805
- [15] GONICHE M. et al., this Conference EX/P5-11
- [16] EKEDAHL A. et al., this Conference
- [17] COLAS L. et al., this Conference
- [18] ALLADIO F. et al., 1994 Plasma Phys. Control. Fusion 36 B253
- [19] CHALLIS C. et al., Nucl. Fusion 60 (2020) 086008 https://doi.org/10.1088/1741-4326/ab94f7
- [20] MAGET P. et al., 47th Conference on Plasma Physics EPS 2021
- [21] YANG X. et al 2020 Nucl. Fusion 60 086012
- [22] SIPS A.C.C. et al 2018 Nucl. Fusion 58 126010
- [23] OSTUNI V. et al., ITPA Transport and Confinement 2020
- [24] SARAZIN Y. et al., this Conference
- [25] MARTIN Y. et al., J. Phys. Conf. Ser. 2008
- [26] VERMARE L. et al., this Conference EX/P5-4
- [27] GASPAR J. et al., this Conference EX/P5-10
- [28] PITTS R.A. et al, Journal of Nuclear Materials 337-339 (2005) 146-153
- [29] FEDORCZAK N. et al., Phys. Scr. T171 (2020) 014046
- [30] GALLO A. et al., Nucl. Fusion 60 (2020) 126048
- [31] CIRAOLO G. et al., this Conference
- [32] TSITRONE E. et al., this Conference
- [33] DE TEMMERMAN G. et al., Plasma Phys. Control. Fusion 60 (2018) 044018

### OV/2-1 1038

- [34] FRELAY F. et al., 2015 Fus. Eng. Des. 98–99 1285–1289
- [35] GROSJEAN A. et al., 2020 Nucl. Fusion in press https://doi.org/10.1088/1741-4326/ab9fa6
- [36] GUNN J.P. et al., Nuclear Materials and Energy 27 (2021) 100920
- [37] DIEZ M. et al., this Conference TECH/P7
- [38] DIEZ M. et al., Nucl. Fusion 60 (2020), 054001
- [39] GUNN J.P. et al., Nucl. Fusion 57 (2017), 046025